sustainability

MDPI

Article

The Effect of Pore Pressure on the Mechanical Behavior of Coal with Burst Tendency at a Constant Effective Stress

Xiaobo Liu [1,2], Kangsheng Xue [1,2,*], Yong Luo [1,2], Kun Long [1,2], Yanan Liu [1,2] and Zhiming Liang [1,2]

[1] State Key Laboratory of Coal Mine Disaster Dynamics and Control, Chongqing University, Chongqing 400044, China
[2] Geofluids, Geomechanics and Geoenergy (3G) Research Group, Chongqing University, Chongqing 400044, China
* Correspondence: ksxue@cqu.edu.cn

Abstract: The mechanical evolution of coal is evident when the pore pressure and the surrounding stress alone influence it. However, the evolution of the mechanical response of saturated coal under the coupling effect of pore pressure and confining pressure needs further investigation. This study identifies the mechanical behaviors of burst tendency dry and saturated coal under the stress condition where confining and pore pressure simultaneously increase but keep the constant difference by conducting a series of triaxial compressions on high burst tendency dry and saturated coal samples. The results show that the elastic modulus (E) and strength (σ_{peak}) of dry coal increase from 3.4 to 4.8 GPa and 78.5 to 92.6 MPa, respectively, and the macro shear failure angle decreases from 64.2° to 56.5° when the confining pressure increases from 9 to 15 MPa. However, these parameters show the opposite evolution law when the pore pressure increases. Furthermore, the E and σ_{peak} of saturated coal decrease from 3.84 to 2.75 GPa and 73.4 to 60.3 MPa, respectively, and the macro shear failure angle of saturated coal increases from 64.7° to 72.4° when the confining pressure and pore pressure increase simultaneously. The coefficient μ is proposed to reveal the evolution of strength at the effective confining pressure. Furthermore, the Mohr–Coulomb failure criterion, including μ, is ameliorated for application in coal under pore pressure conditions. In addition, a model was developed to reveal the effect of a pore-rich layer on the angle of macrocracks, which was confirmed by acoustic emission. The research reveals the mechanical behavior of coal under high pore pressure. Improved Mohr–Coulomb criterion criteria provide new guidance and vision for the analysis of coal instability in high pore pressure coal seams.

Keywords: pore pressure; constant effective stress; elastic modulus; strength; coal

Citation: Liu, X.; Xue, K.; Luo, Y.; Long, K.; Liu, Y.; Liang, Z. The Effect of Pore Pressure on the Mechanical Behavior of Coal with Burst Tendency at a Constant Effective Stress. *Sustainability* **2022**, *14*, 14568. https://doi.org/10.3390/su142114568

Academic Editor: Baoqing Li

Received: 4 October 2022
Accepted: 2 November 2022
Published: 5 November 2022

1. Introduction

Compound dynamic disasters have been exposed in mining strong adsorption and low permeability coal seams in China [1,2]. The compound dynamic disasters are not only single conventional coal and gas outbursts or coal burst disasters, but also the combination of the two conventional coal dynamic disasters [3–5]. To prevent compound dynamic disasters, it is essential to ascertain the occurrence mechanism of compound dynamic disasters. The role of pore pressure in disasters is different from that in coal and gas outbursts [6,7]. In conventional coal burst hazards, the role of pore pressure is not considered. However, in compound dynamic disasters, pore pressure plays a new role. The effect of pore pressure in coupling coal and gas dynamic disasters has attracted widespread interest [8–11]. A deep understanding of the role of pore pressure in high burst tendency coal seams is imperative to reveal the mechanism of compound dynamic disasters and avoid compound dynamical disaster occurrence.

Coal is a geological rock that contains abundant pores and fissures [12]. These pores and fissures in coal provide storage space for geological fluids [13,14]. In the shallow part

of the coal seam, the ground stress in the coal seam is low, and the coal seam permeability is high. Geological fluids, such as methane and carbon dioxide, can escape to the atmosphere over a long geological period of time. As the depth of coal mining increases, the coal seam confining stress significantly increases [15]. The permeability of the coal seam is also significantly reduced [16–18]. A large amount of geological fluid is adsorbed in the pores of the coal seam. Consequently, the pore pressure of the geological fluids in the coal seam increases significantly. Higher pore pressure has a visible effect on the mechanical properties of coal [19]. The strength and elastic modulus of coal are two critical mechanical parameters [20]. The elastic modulus is usually used to reflect the deformation and to evaluate the accumulation of elastic energy [21], and strength characteristics are also crucial for coal damage. Studies have shown that the elastic modulus and strength increase when the coal confining stress increases [22,23]. For example, the strength increases from 61.6 MPa to 129.7 MPa, and the elastic modulus increases from 4.77 to 6.88 GPa when the burial depth increases from 300 m to 1050 m in the Pingdingshan coal mine [24]. In contrast, the effect of pore pressure on the mechanical properties is opposite to that of confining stress. The pore pressure of geological fluids such as water and carbon dioxide decreases the elastic modulus and strength [25,26]. As a result, the evolution trends of the elastic modulus and strength are complicated when the increases in the burial depth lead to a simultaneous increase in the pore and confining stress.

The effective stress concept was proposed to consider the combined effect of pore pressure and external pressures. The effective stress [27] is defined as

$$\sigma^{e} = \sigma - p \tag{1}$$

where σ^{e} is the effective stress, σ is the total stress (external pressures), and p is the pore pressure. Biot further promoted the concept of the effective stress coefficient α [28].

$$\sigma^{e} = \sigma - \alpha p \tag{2}$$

Effective stress has been widely used for rock and coal [29,30]. The effective stress is of greater concern as it represents the true stress in the coal when the coal is subjected to total stress and pore pressure. According to Equation (1), an increase in total stress leads to an increase in effective stress; i.e., the effect of the total stress can be reflected by the effective stress when the pore pressure is constant. However, effective stress is a binary function of pore pressure and total stress. The representation of effective stress becomes complex when both the pore pressure and the total pressure increase by the same magnitude. For example, assuming a pore pressure of 1 MPa and total stress of 4 MPa at shallow depths and a pore pressure of 27 MPa at deeper depths, the total stress is 30 MPa. The two distinctly different total stress and pressure conditions have the same effective stress of 3 MPa. The evolution of the mechanical parameters of coal, such as the strength and elastic modulus, is not known when the pore and envelope pressures increase simultaneously, resulting in constant effective stress. Therefore, this study investigates the effect of constant effective stress on the mechanical behavior of coal due to a simultaneous increase in total stress and pore pressure.

2. Materials and Methods

2.1. Test Apparatus

Triaxial compression tests were conducted using the MTS 815 mechanical system, which has a maximum axial load of 2800 kN and a maximum confining pressure of 80 MPa, and axial and radial extensometers with a resolution ratio of 0.0001 mm. A schematic diagram of the pore pressure test by MTS 815 is shown in Figure 1. The PCI-2 acoustic emission system was used to monitor crack development in coal. The maximum signal amplitude is 100 dB, and the minimum threshold of AE acquisition is 17 dB. The threshold of AE acquisition was set to 35 dB. Nuclear magnetic resonance (NMR) analysis can cover the pore and crack sizes of coal [31]. The MacroMR12-150H-I system produced

by Newman Electronic Technology Co., Ltd. (2014) (Suzhou, Jiangsu, China) was used to measure the porosity in coal. All test equipment used is from the State Key Laboratory of Coal Mine Disaster Dynamics and Control, Chongqing, China, where we conducted all the experiments.

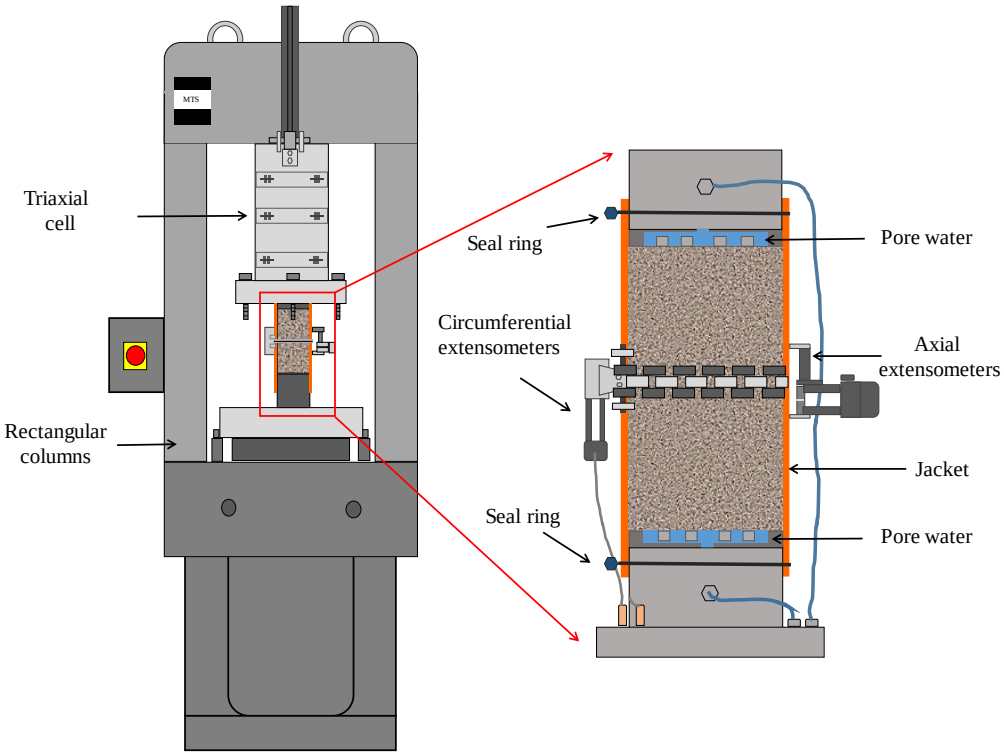

Figure 1. Schematic diagram of the compressive pressure tests by MTS 815.

2.2. Samples

In this paper, the coal blocks were obtained from the Tingnan (TN) and Zhengtong (ZT) collieries in Xianyang city, Shannxi Province, China, as shown in Figure 2a. The coal blocks from the two collieries were both from the 4# coal seam in the Yan'an Formation, Jurassic period. The depth of burial of the ZT coal seam is 581.5–1195.5 m. The average thickness of the coal seam is 9.02 m. The depth of burial of the seam is 600–700 m, where the coal samples were taken. The maximum gas content of the drilled seam is 2.91 m^3/t. The maximum gas content of the surrounding rock is 4.76 m^3/t. The water content of the rock beneath the Zhengtong coal seam is weak and can be regarded as a relative water barrier. The direct water-filled aquifer of the coal seam is the sandstone fissure aquifer of the Jurassic Middle Formation Zhiluo Group and the coal seam of the Jurassic Middle Formation Yan'an Group and its roof sandstone aquifer, and the water-filling method is the roof inlet. The indirect water-filled aquifer is the Lower Cretaceous sand and gravel aquifer, which is infiltrated along the fracture penetration section. The normal water surge in the mine is 847 m^3/h.

The depth of burial of the coal seam at the TN colliery was 581.5–1195.5 m. The average thickness of the coal seam was 10.75 m. The depth of burial of the coal sample was 650–800 m. The maximum gas content of the drilled seam was 4.03 m^3/t. The maximum gas content of the surrounding rock is 0.54 m^3/t. The direct water-filled aquifers of the TN 4# coal seam are the Cretaceous Luohe Group and Yijun Group aquifers, the Jurassic Zhiluo Group aquifers, and the Yan'an Group aquifers, which are weakly water-rich. The water from the Cretaceous Luohe Formation aquifer is the main source of water threatening the safety of the mine. The aquifer is moderately water-rich, has a large thickness, and is mainly recharged by regional lateral runoff, with average recharge conditions. The overall

assessment is moderate, with an expected normal surge of 360 m^3/h and a maximum surge volume of 560 m^3/h. The coalfield has simple geological formations with few faults. The coal seam stresses of the two collieries are mainly overlying gravity.

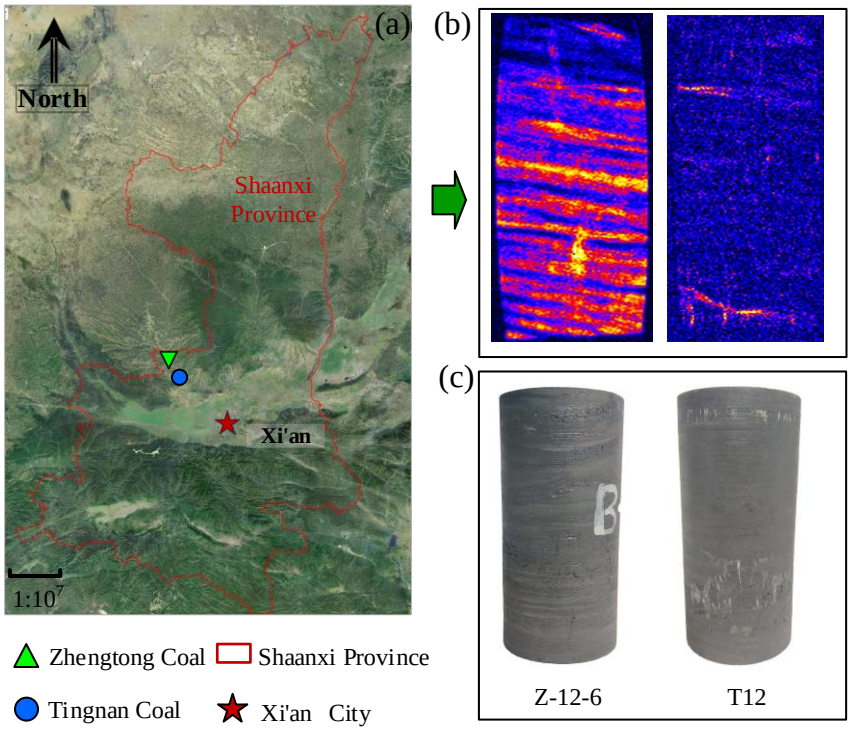

Figure 2. (**a**) Location of the coal mine; (**b**) NMR slice graph of the coal sample: T12 (right) and Z-12-6 (left). The blue area denotes the coal matrix, the red area denotes a minor porosity, and the yellow area denotes a large porosity; (**c**) TN and ZT coal samples.

The coal blocks from the ZT colliery have relatively higher porosities, ranging from 6% to 10%; the coal blocks from the TN colliery have lower porosities, ranging from 2% to 6%. Furthermore, the significant differences between the two kinds of coal are in pore structure and size distribution. Figure 2b shows the pore structure of the high-porosity coal sample Z-12-6 (left) and low-porosity coal sample T12 (right). The blue area denotes the coal matrix, the red area denotes micropores (<2 nm), and the yellow area denotes large macropores (>50 nm) [32]. Z-12-6 contains many approximately horizontal porosity layers. In contrast, T12 has few horizontal porosity layer planes. Figure 3 shows the pore size distribution of the representative coal samples from the two collieries. The pore size range for both coal samples is from 5×10^{-4} μm to 50 μm. However, the pore size distribution curve of the low-porosity TN coals has a larger peak and a smaller peak. Pores smaller than 0.1 μm make up the majority of the TN coal, which indicates a relatively uniform pore size distribution of the coal. The pore size distribution curve for the ZT coal has two equal wave peaks. The presence of two major pore size magnitudes indicates the porous-rich layer band in the ZT coal.

Cylindrical coal cores 50 mm in diameter were drilled from the blocks in the vertical drilling direction to the layer plane of coal. Then, the cylinder coal cores were cut short to approximately 101 mm in height. The two ends of the coal core were carefully polished to the final height of the core, approximately 100 mm. In total, fifty coal samples conforming to the standard of ISRM [33] were prepared. The coal samples were dried in an oven at 60 °C for 24 h before the compression tests.

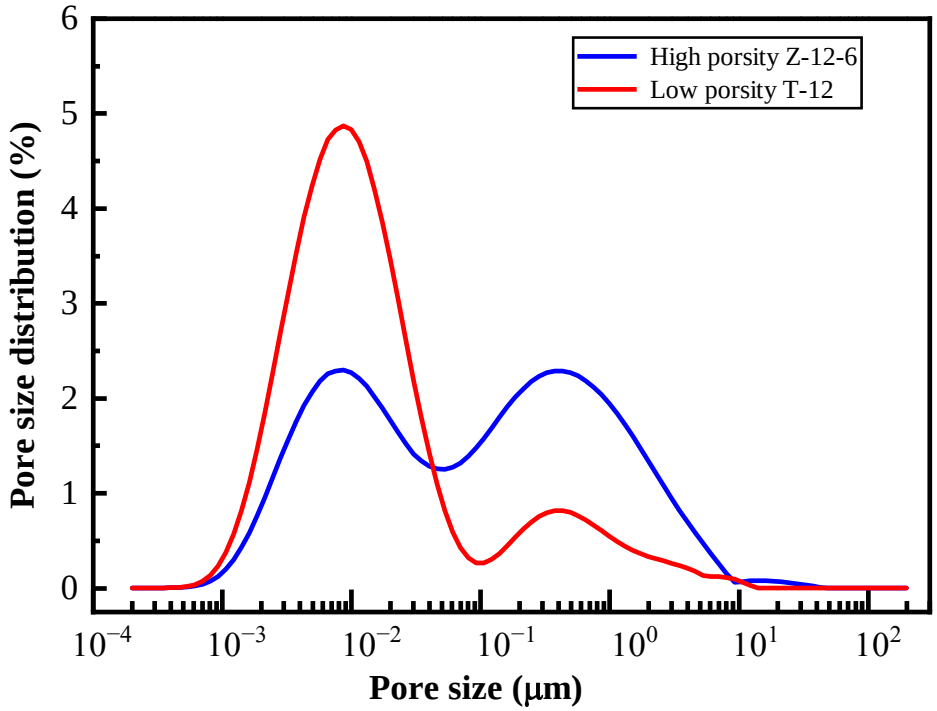

Figure 3. Pore size distribution of representative TN and ZT coal samples.

2.3. Testing Methods

Prior to the triaxial compression test, 12 coal samples were saturated with distilled water at 5 MPa hydrostatic pressure for 2 h. Then, the coal samples were subjected to NMR monitoring to determine the pore size distribution and porosity. Finally, the coal samples were loaded during mechanical tests. The stress path of the triaxial compression test is as follows: axial stress and confining pressure were loaded to preset pressure at a stress rate of 3 MPa/min. Then, the pore pressure was increased to the preset pore pressure at the same stress rate when the axial stress and confining pressure were stable. Then, the pore pressure was maintained for 30 min to thoroughly saturate the coal sample and ensure pore pressure stability. Finally, the axial load was increased at 0.5 mm/min until the coal samples failed.

The mechanical test section consists of two main categories: one group of conventional triaxial compression experiments using dry and wet coal samples under no pore pressure conditions, and another group of triaxial compression experiments with loaded pore pressure using saturated coal samples under drained conditions. It should be noted that no pore pressure was added during experiments with dry and wet specimens, while pore pressure was added during experiments with saturated specimens. Both experiments were set up with three confining pressures of 9, 12, and 15 MPa. In the experiments with loaded pore pressures, two pore pressures were set at each confining pressure so that the confining pressure minus the pore pressure was equal to 3 or 6 MPa. This gives different confining pressures, σ_3, and pore pressures, P_P, but the same effective confining stress, $\sigma^e{}_3$ (the constant effective confining stress). The details of the pressure of the coal sample are shown in Table 1. The specimens are numbered using a letter plus numbers. The letters Z and T indicate if the coal samples were obtained from the ZT or TN coal mine, respectively. In the name of the specimen, the middle number represents the confining pressure, and the left number represents the pore pressure.

Table 1. The pressure and porosity of the coal samples.

Sample Name	σ_3 MPa	P_P MPa	Porosity %	Condition	Sample Name	σ_3 MPa	P_P MPa	Porosity %	Condition
Z-9-3	9	3	7.29	Saturated	T-9-3	9	3	2.58	Saturated
Z-9-6	9	6	8.70	Saturated	T-12-6	12	6	4.05	Saturated
Z-12-6	12	6	6.89	Saturated	T-15-9	15	9	5.20	Saturated
Z-12-9	12	9	7.69	Saturated	Z-9	9	0	6.86	Dry
Z-15-9	15	9	8.17	Saturated	Z-12	12	0	9.66	Dry
Z-15-12	15	12	6.83	Saturated	Z-15	15	0	9.49	Dry
Z-12-0	12	0	7.78	Wet	Z-9-0	9	0	9.07	Wet
Z-15-0	15	0	6.55	Wet					

Note: σ_3 is the confining pressure; P_P is the pore pressure.

2.4. AE Analysis Methods

The AE technique has been widely used in the process of material damage analysis [34]. AE parameter analysis [35,36] has been used to identify the type of crack development in coal samples. This method uses two AE parameters, the average frequency (AF) and RA, where a shear crack is characterized by a low AF and a high RA; in contrast, a tensile crack is characterized by a high AF and a low RA [36,37], as shown in Figure 4. The parameters RA and AF can be obtained as follows.

$$RA = Rise\ time / the\ amplitude \quad (3)$$

$$AF = Ringdown\ count / the\ duration\ time \quad (4)$$

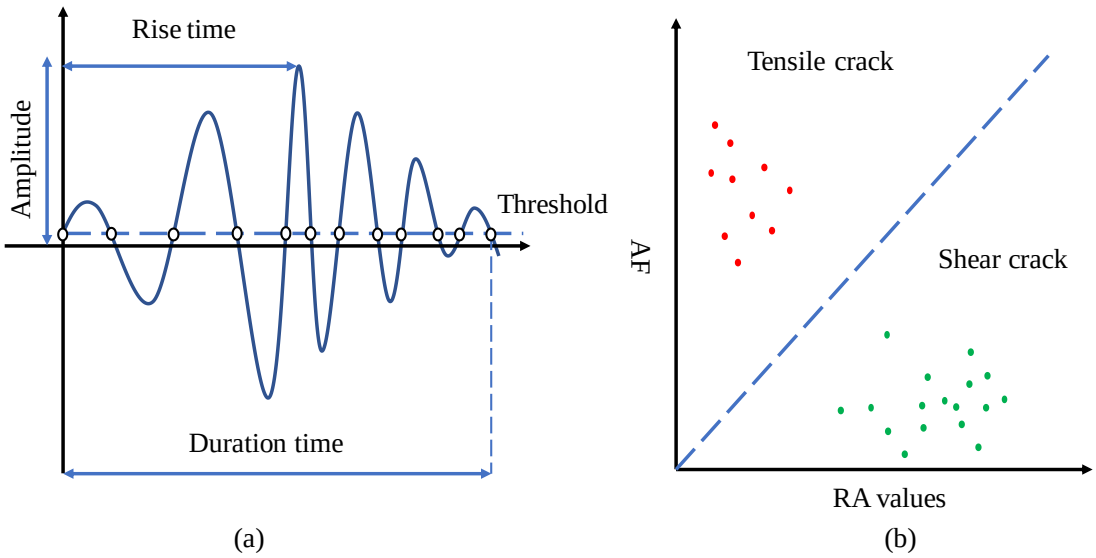

Figure 4. AE analysis: (**a**) AE wave and parameters; (**b**) schematic of AE parameter analysis of crack classification.

3. Experimental Results

3.1. Effect of Pore Pressure on the Stress–Strain Curves

Stress–strain curves are the direct reflection of the mechanical response of coal samples under certain stress conditions. Typical coal will present five deformation stages: crack closure, elastic region, stable crack growth, unstable crack growth, and post-peak stages under compression [38,39]. The differential stress–axial strain curves of the coal samples are shown in Figure 5. The axial strain curves of the coal samples at pore pressures of 3, 6, 9 and 12 MPa are shown in Figure 5a–c, respectively. The results show that the stress–axial strain curve with the lower pore pressure is greater than the stress–axial strain curve with

the higher pore pressure. This suggests that pore pressure decreases the slope of the curves. Furthermore, under the σ^e_3 = 6 MPa condition (Figure 5d), the slope of the curves decreases as σ_3 and P_P increase simultaneously. Figure 5e,f show the differential stress–axial strain curves of dry and saturated coal samples without preset pore pressure. The slope of the curves increases as σ_3 increases. Comparing Figure 5a,e, it can be seen that the effect of σ_3 on the axial strain curve is opposite of that of the pore pressure.

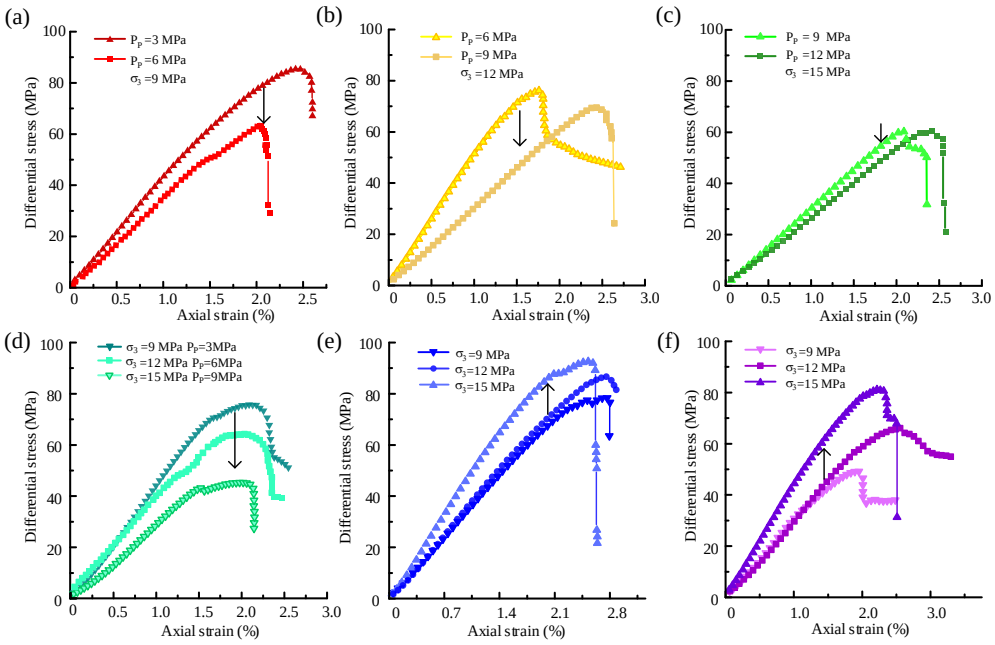

Figure 5. Differential stress–axial strain curves of the coal samples: (**a**–**c**) ZT coal sample at 3 and 6 MPa effective confining pressures; (**d**) TN coal sample at an effective confining pressure of 6 MPa; (**e**) dry coal sample; (**f**) wet coal sample without a preset pore pressure.

The differential stress–radial strain curves of the coal samples are shown in Figure 6. The slope of the linear segment (strain < 0.5% in Figure 6a) of the radial strain curve for the dry coals increases with increasing confining pressure when no pore pressure is applied. This indicates that the confining pressure limits the lateral expansion of the coal sample. In addition, the radial strain curves in Figure 6a have a distinct unstable crack growth stage and post-peak stage, which is also different from Figure 6b. When the coal samples are subjected to pore pressure, the slope of the linear part of the radial strain curve before the peak stress decreases as the pore and confining pressures increase in parallel, as shown in Figure 6b. This is in contrast to the evolution of the curve of dry coal, indicating that the effect of the pore pressure on the radial strain is greater than that of the confining pressure on the radial strain when the pore pressure and the confining pressure are increased simultaneously. As shown in Figure 6b, the linear part of the radial strain curve before the peak stress increases significantly, the nonlinear part decreases when the pore pressure increases, and the confining pressure increases. Even at pore pressures of 6 and 9 MPa, the radial strain curve exhibits a straight line before the peak stress. This indicates that the unstable crack growth stage of the coal decreases and that coal is dominated by the elastic and stable crack growth stages under the effect of pore pressure. Furthermore, the post-peak curve collects less valid data, and there is almost no post-peak portion. This indicates that unstable failure of the coal has occurred.

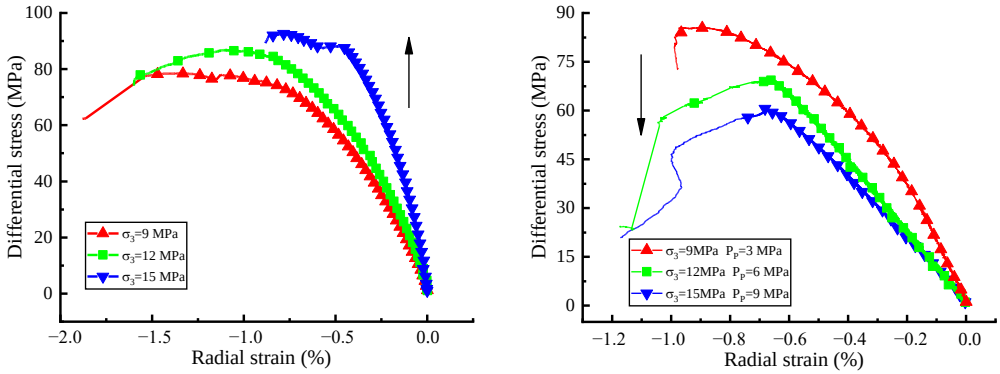

Figure 6. Differential stress–radial strain curves of the coal samples at confining pressures of 9, 12, and 15 MPa: (**a**) dry coal samples; (**b**) saturated coal sample at $\sigma^{e}{}_{3}$ = 6 MPa.

The strain of the peak stress (ε_{peak}) and damage stress (ε_{cd}) in the curve have a critical exponential role in the deformation of the coal. ε_{peak} indicates the strain of coal before macro failure. ε_{cd} is the inflexion point in a volumetric strain curve and suggests a shift from the volume compression to volume expansion of the coal. Figure 7 shows the stress–volumetric strain curves of the dry coal samples and wet coal samples without preset pore pressure. The stress–volumetric strain curves exhibit a semilunar shape, which is a very common feature. ε_{peak} is at the top of the curve and is also less than ε_{cd}. The volume–strain curve between ε_{cd} and ε_{peak} indicates that the coal samples enter the yield stage and begin to deform plastically and expand volumetrically. The ε_{cd} of the dry coal sample increases 70% with an increase in confining pressure from 9 to 15 MPa. This suggests that the maximum volumetric compression of a dry coal sample is positively correlated with confining pressure; i.e., the strain at ε_{cd} increases with an increase in σ_3. Furthermore, the ε_{cd} of the wet coal sample increases by 67%. The ε_{cd} evolution of the wet coal sample coincides with that of the dry coal sample, while both the values and increase in ε_{cd} are lower than those of the dry coal samples.

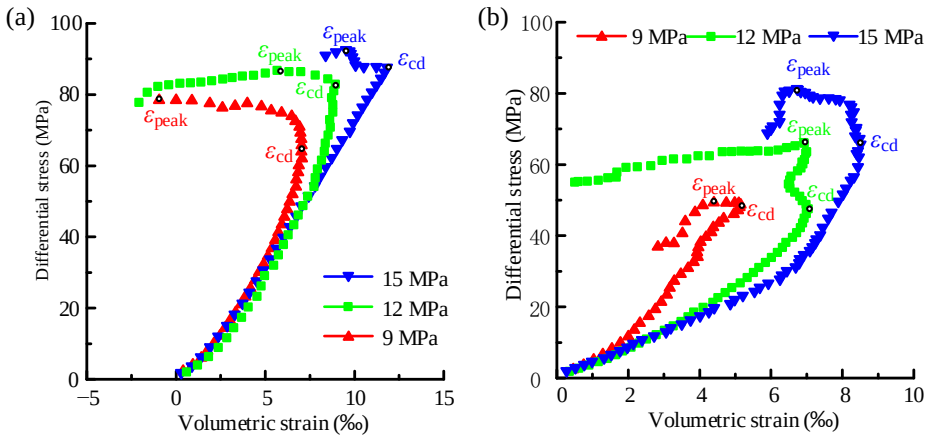

Figure 7. Differential stress–volumetric strain curves of the coal samples at confining pressures of 9, 12, and 15 MPa: (**a**) dry coal samples; (**b**) wet coal samples without a preset pore pressure.

The volumetric strain curve of coal under pore pressure rarely exhibits a semilunar shape and is closer to a linear line, as shown in Figure 8. This is the distinctive feature of the volumetric stress–strain under the effect of pore pressure. In the linear line volumetric strain curve, ε_{peak} is equal to ε_{cd}, not less than ε_{cd}. This indicates that the yield stage of high burst tendency coal is short or even nonexistent under the effect of pore pressure. Figure 8a–c show the ε_{cd} of saturated coal samples at confining pressures of 9, 12, and

15 MPa with an increase in pore pressure, respectively. ε_{cd} increases with an increase in pore pressure; e.g., ε_{cd} increases from 4.6‰ to 10.6‰ when the pore pressure is increased from 6 to 9 MPa (Figure 8b). This indicates that the strain of ε_{cd} increases with a decrease in the effective confining pressure. This evolution of ε_{cd} of saturated coal at an increased effective confining pressure is opposite to that of dry coal with an increase in confining pressure. Figure 8d shows that ε_{cd} increases from 8.21‰ to 10.4‰ when the confining pressure and pore pressure are increased to maintain a constant effective confining pressure of σ^e_3 = 3 MPa. In addition, ε_{epak} is equal to ε_{cd} and increases with increasing σ_3 and P_P, which represents a reduction in plastic deformation before ε_{peak}.

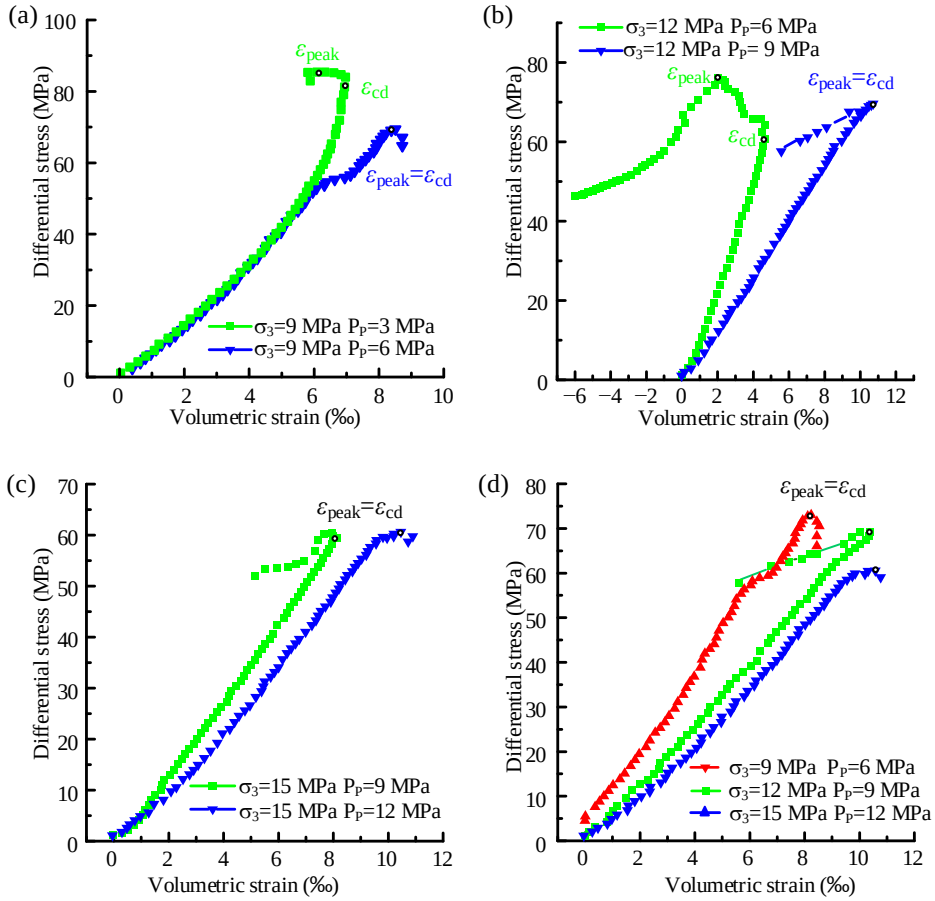

Figure 8. Differential stress–volumetric strain curves of coal samples: (**a**) σ_3 = 9 MPa; (**b**) σ_3 = 12 MPa; (**c**) σ_3 = 15 MPa; (**d**) σ^e_3 = 3 MPa.

3.2. Effect of Pore Pressure on Elastic Modulus

The elastic modulus (E) not only reflects the deformation ability of coal but also relates to the storage of strain energy. In this paper, E is acquired according to the linearity of the differential stress–axial strain curves. E is calculated by Equation (5).

$$E = \frac{\Delta\sigma_1}{\Delta\varepsilon_1} \tag{5}$$

where $\Delta\sigma_1$ and $\Delta\varepsilon_1$ denote the difference between σ_1 and ε_1. Figure 9a shows that the E of dry coal samples increases from 3.4 to 4.8 GPa with an increase in confining pressure from 9 to 15 MPa. The evolution of E of the wet coal samples shows an increasing tendency that is extremely similar to that of the dry coal samples. However, the E of the wet coal samples is lower than that of the dry coal samples at each confining pressure. This suggests that pore water has a weakening effect on the elastic modulus. Figure 9b shows that E decreases with

an increase of 3 MPa in pore pressure when the coal sample is at each confining pressure (9, 12, and 15 MPa). Figure 9c shows the evolution of the E of the TN coal samples. E decreases from 4.65 to 3.12 GPa at the constant effective confining pressure of σ^e_3 = 6 MPa. It can be summarized that the E of the dry coal will increase with increasing confining pressure. However, the E of saturated coal will decrease as pore pressure increases. Furthermore, the E of the coal samples decreases with increasing P_P and σ_3 but at a constant σ^e_3.

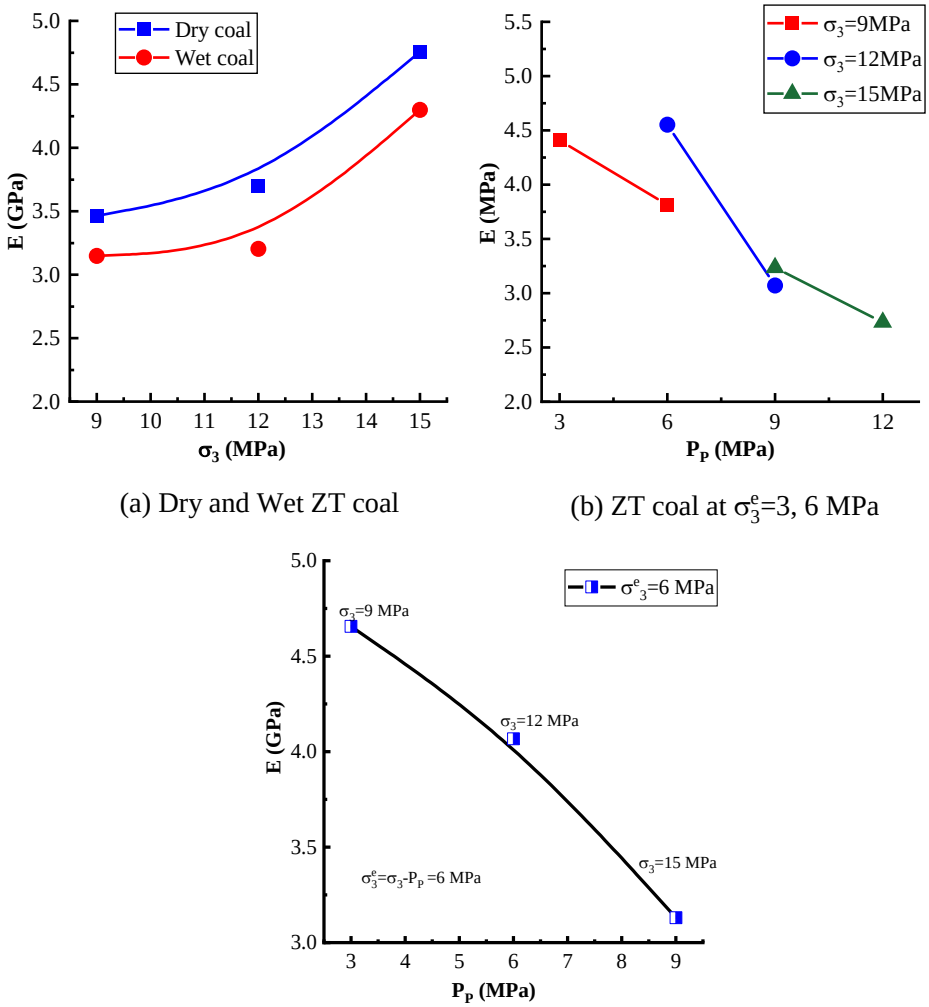

(a) Dry and Wet ZT coal

(b) ZT coal at σ^e_3=3, 6 MPa

(c) TN coal at σ^e_3=6 MPa

Figure 9. Elastic modulus evolution of the coal samples: (**a**) dry coal and wet coal samples without pore pressure; (**b**) saturated coal samples at effective confining pressures of 3 and 6 MPa; (**c**) saturated TN coal samples at an effective pore pressure of 6 MPa.

3.3. Effect of Pore Pressure on Strength and the Coefficient μ

3.3.1. Strength and Mohr's Stress Circle Characteristics in the Absence of Pore Pressure

The peak stress (σ_{peak}), damage stress (σ_{cd}), and crack initiation stress (σ_{ci}) are three mechanical parameters of great importance in coal mechanics. σ_{peak} is the strength of the coal and represents the maximum stress value at the coal failures. σ_{cd} is the yield strength of the coal, also known in engineering practice as long-term strength. σ_{ci} is the elastic limit of the coal. Beyond this stress, microcracks begin to initiate, and the coal material is damaged [39]. Figure 10 shows the three stresses of the dry and wet coal samples. The σ_{peak} of the dry coal sample increases from 78.5 to 92.6 MPa, and the σ_{peak} of the wet coal samples increases from 51.7 to 81.5 MPa when σ_3 increases from 9 to 15 MPa. The increasing tendency in σ_{peak} with increasing σ_3 meets the classical Mohr–Coulomb criterion

and can be expressed by a linear function. It should be noted that the pore water damaged the microstructure of the wet coal sample under undrained conditions, which caused a significant σ_{peak} difference between the dry coal sample and the saturated coal at the same confining pressure.

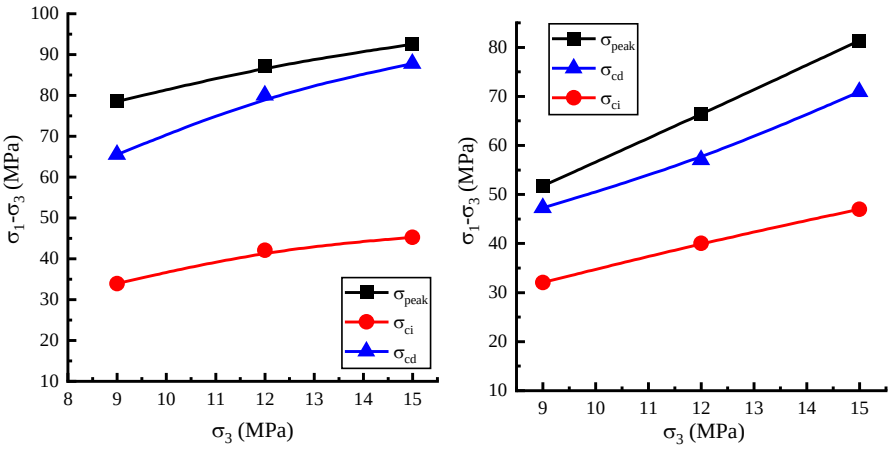

Figure 10. Triaxial compressive strength of the dry and wet coal samples.

The ratio of σ_{ci} to σ_{peak} for the dry coal ranges between 0.43 and 0.58, while the ratio of σ_{ci} to σ_{peak} for the wet coal ranges between 0.58 and 0.62. The comparison shows that the ratio of σ_{ci} to σ_{peak} of the dry coal is less than the wet coal rock ratio. However, there is no significant σ_{ci} difference between the dry and wet coal at each σ_3. The ratio of σ_{ci} to σ_{peak} of the dry coal is lower than that of the wet coal due to the σ_{peak} of the wet coal rock being lower than that of dry coal. In addition, comparing the σ_{cd} of the dry and wet coal shows that pore water reduces the σ_{cd} stress, contributing to the coal entering the yielding stage early.

The Mohr–Coulomb criterion is one of the most widely used strength criteria in rock engineering practice. The criterion indicates that the failure is mainly due to the shear stress τ on the failure surface being greater than its shear strength. The shear strength is related to the normal stress σ_n on the failure surface. The Mohr–Coulomb criterion is shown in Equation (6):

$$\tau = c + \sigma_n \tan\phi \quad (6)$$

where c is cohesion and φ is the internal friction angle.

According to the stress of the dry and wet coal samples at no preset pore pressure, Figure 11 shows the Mohr circle envelopes. The envelope of the dry coal samples can be expressed by Equation (7) as follows:

$$\tau = 16.44 + \sigma_n \tan(27.14) \quad (7)$$

The cohesion and the internal friction angle of the dry coal sample are 16.44 MPa and 27.14° based on Mohr's circle envelope. Furthermore, the envelope of the wet coal samples can be expressed by Equation (8). Comparing Equations (7) and (8), there is a significant difference between the dry and wet coal samples in internal friction angle and cohesion. The pore water reduces the cohesion of coal by 84%, while the angle of internal friction increases by 67%.

$$\tau = 2.54 + \sigma_n \tan(45.29) \quad (8)$$

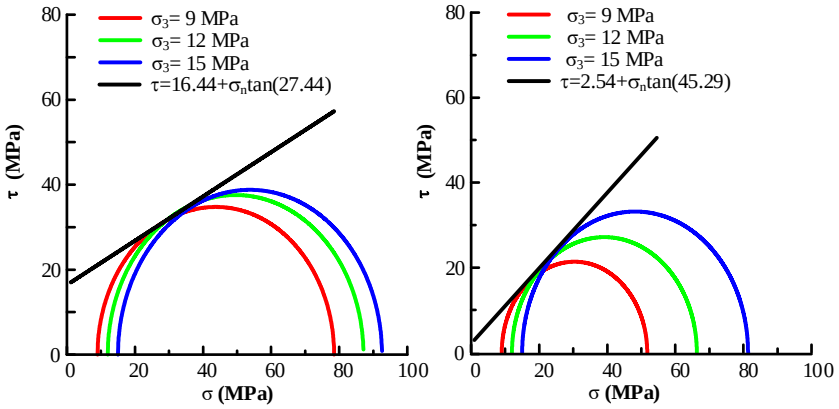

(a) Dry (b) Wet

Figure 11. Mohr's circle and strength envelopes.

Based on rock and elastic mechanics, the shear stress and normal stress on the failure plane are expressed by Equation (9):

$$\left.\begin{array}{c} \sigma_{\mathrm{n}} = \frac{\sigma_1+\sigma_3}{2} + \frac{(\sigma_1-\sigma_3)}{2}\cos(2\beta) \\ \tau = \frac{(\sigma_1-\sigma_3)}{2}\sin 2\beta \end{array}\right\} \quad (9)$$

where τ is the shear stress on the failure plane, σ_{n} is the normal stress on the failure plane, and β is the degree between the maximum principal stress and the normal direction on the failure plane. Substituting Equation (9) into (6), the Mohr–Coulomb criterion can be derived by the form of the minimum and maximum principal stresses, as shown in Equation (10), where σ_1 and σ_3 are *the* total stresses. The calculation of Equation (10) is listed in Appendix A. It is clear that σ_1 and σ_3 have a positive correlation and a single value relationship and that the unique σ_3 has the unique σ_1.

$$\sigma_1 = \sigma_3 + \frac{2(\mathrm{c} + \sigma_3 \tan\phi)}{(1 - \tan\phi\cot\beta)\sin 2\beta} \quad (10)$$

3.3.2. Stress Analysis under the Effect of Pore Pressure

When coal is subjected to pore pressure P_{P}, substituting Equation (1) into (9), the normal and shear stress on the failure surface is obtained as follows.

$$\left.\begin{array}{c} \sigma_{\mathrm{n}} = \frac{\sigma_1+\sigma_3}{2} + \frac{(\sigma_1-\sigma_3)}{2}\cos 2\beta - P_{\mathrm{p}} = \frac{\sigma^{\mathrm{e}}{}_1+\sigma^{\mathrm{e}}{}_3}{2} + \frac{(\sigma^{\mathrm{e}}{}_1-\sigma^{\mathrm{e}}{}_3)}{2}\cos 2\beta \\ \tau = \frac{(\sigma_1-\sigma_3)}{2}\sin 2\beta = \frac{(\sigma^{\mathrm{e}}{}_1-\sigma^{\mathrm{e}}{}_3)}{2}\sin 2\beta \end{array}\right\} \quad (11)$$

By comparing Equations (9) and (11), it can be seen that the normal stress σ_{n} is reduced by P_{p}. The maximum and minimum principal stresses decrease by pore pressure, leading to a left horizontal movement of Mohr's circle on the abscissa axis, but the diameter of the Mohr's circle is a constant, as shown in Figure 12a. This is the conventional schematic diagram of the effect of pore pressure on Mohr's circle. Furthermore, the mathematical expression for this stress relationship is $\sigma_1 = m\sigma_3 + k$, where $m = 1$ and k is a constant. However, the results of this study show that the effect of pore pressure on Mohr's circle is not only a left horizontal movement but also causes the shape of the Mohr's circle to be small (Figure 12b). For instance, the diameter of the Mohr's stress circle decreases from 77 to 67 when loaded with $P_{\mathrm{P}} = 9$ MPa, while the diameter should remain at 77, according to Figure 12a. This result significantly indicates that the evolution of Mohr's circle shape is not only horizontal movement but also smaller due to the pore pressure effect (Figure 12c). This means that m in the equation $\sigma_1 = m\sigma_3 + k$ is greater than 1. Since m is greater than 1, the weakness of σ_1 will be more pronounced than σ_3 when the coal sample is under

pore pressure. Therefore, we propose a new schematic representation of the action of pore pressure on Mohr's circle, as shown in Figure 12c.

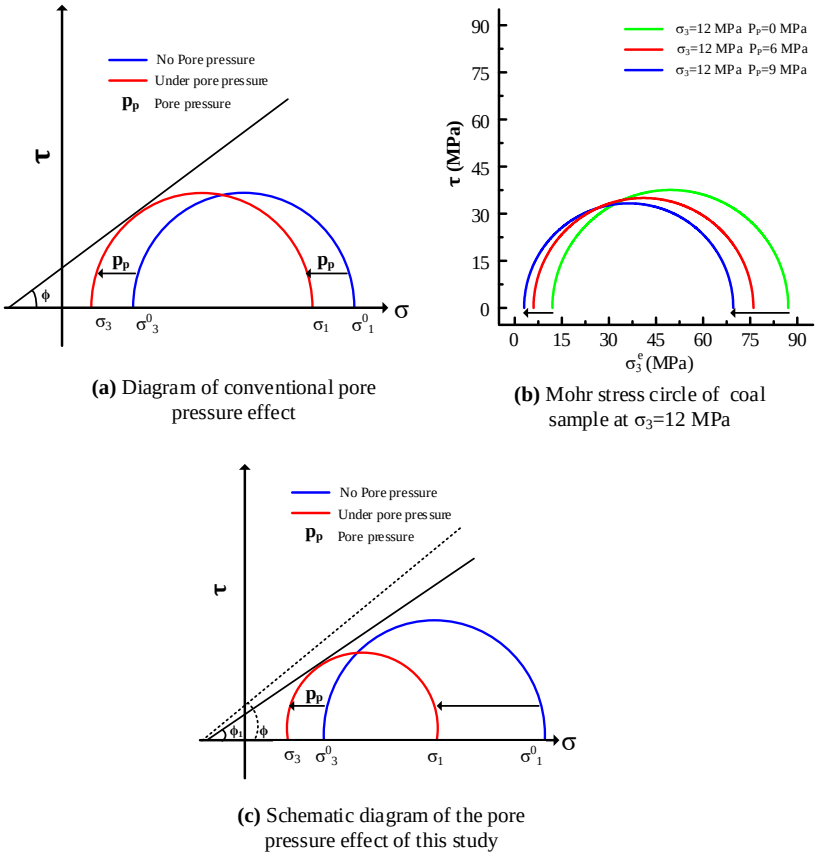

(a) Diagram of conventional pore pressure effect

(b) Mohr stress circle of coal sample at σ_3=12 MPa

(c) Schematic diagram of the pore pressure effect of this study

Figure 12. Schematic diagram of the effect of pore pressure on the Mohr circle: (**a**) conventional schematic diagram of the pore pressure; (**b**) Mohr circle of the coal samples at P_P = 0, 6, and 9 MPa, and σ_3 = 12 MPa; (**c**) schematic diagram of the pore pressure in this study. $\sigma_{1,3}$ denotes the maximum and minimum principal stresses under pore pressure. $\sigma^0{}_{1,3}$ denotes the initial state of the maximum and minimum principal stresses in the absence of pore pressure.

3.3.3. Multivalued Strength Characteristics under Pore Pressure

The effect of pore pressure change on coal strength is analyzed when σ_3 is fixed. The following is an analysis of the effect on coal strength when both σ_3 and P_P increase simultaneously, but the difference ($\sigma^e{}_3$) between σ_3 and P_P is constant. Figure 13 shows the two strength characteristics of the coal samples at constant effective confining pressures of $\sigma^e{}_3$ = 3 and 6 MPa. The first is that the strength of the coal sample increases as $\sigma^e{}_3$ increases from 3 to 6 MPa. For example, the strength increases from 73.1 to 85.3 MPa when the ZT coal samples are at a confining pressure of 9 MPa, as shown in Figure 13a. This is in accordance with the Mohr–Coulomb criterion. The second characteristic is that the strength decreases with increasing σ_3 and P_P, and it should be noted that the effective confining pressure is fixed at this point. For example, the strength of the saturated ZT coal samples decreases from 85.3 to 62.76 MPa when the coal samples are at the effective confining pressure of 6 MPa. Furthermore, the Mohr stress circle at the constant effective stress is shown in Figure 14. When the effective stress is certain, the diameter of the Mohr circle stress circle decreases with increasing σ_3 and P_P.

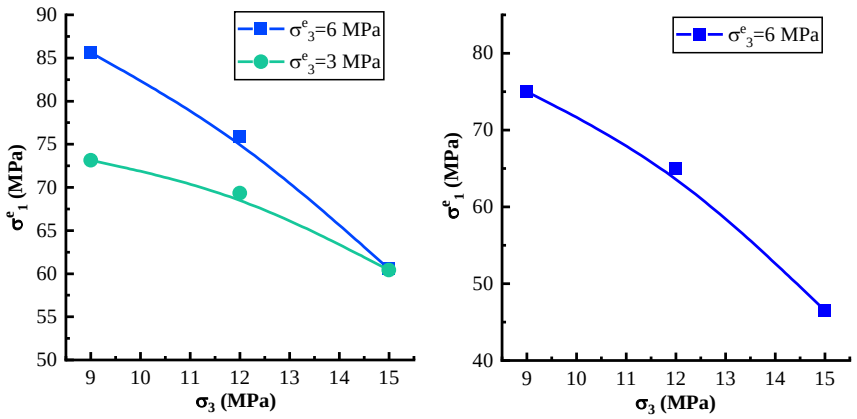

(a) Saturated coal from ZT coal mine (b) Saturated coal from TN coal mine

Figure 13. Strength of the saturated coal samples at 3, 6, and 9 MPa pore pressure: (**a**) saturated ZT coal samples at σ^e_3 = 3 and 6 MPa; (**b**) saturated TN coal samples at σ^e_3 = 6 MPa. σ^e_3 denotes the effective confining pressure and equals the confining pressure minus the pore pressure.

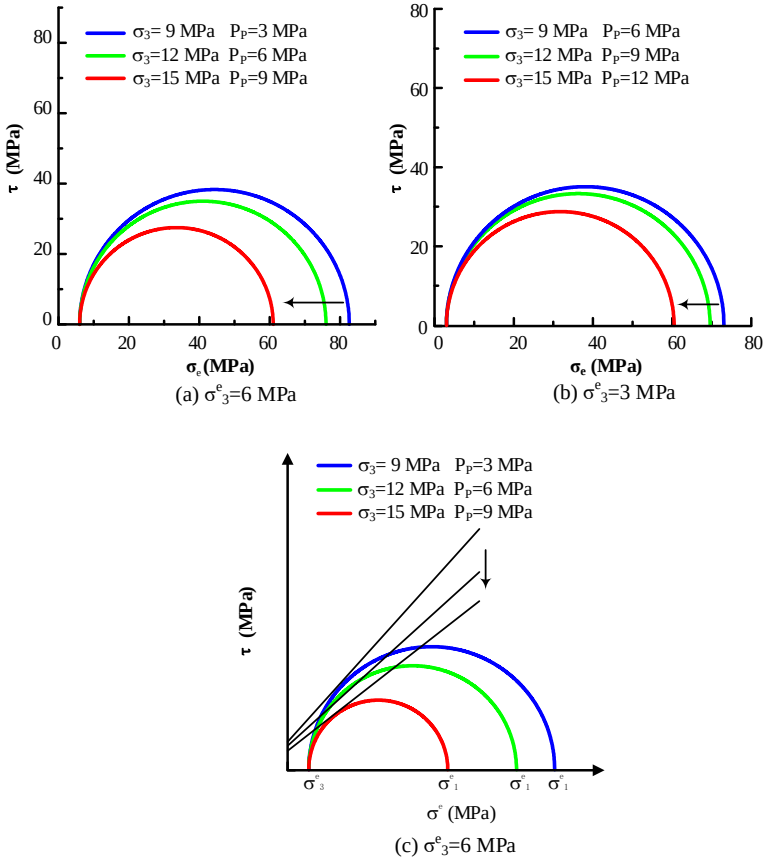

(a) σ^e_3=6 MPa (b) σ^e_3=3 MPa

(c) σ^e_3=6 MPa

Figure 14. Mohr's circle of the saturated coal sample at constant effective confining pressures: (**a**) coal samples at σ^e_3 = 6 MPa; (**b**) coal samples at σ^e_3 = 3 MPa; (**c**) schematic representation of the Mohr circle and yield criterion at constant effective stress.

Equation (12) considers the conventional Mohr–Coulomb criterion and effective stress pressure. Equation (12) is obtained by substituting Equation (11) into Equation (6).

$$\sigma^e_1 = \sigma^e_3 + \frac{2(c + \sigma^e_3 \tan\phi)}{(1 - \tan\phi \cot\beta)\sin 2\beta} \quad (12)$$

Equation (12) suggests a positive relationship between the maximum and minimum effective principal stresses. However, this equation cannot explain the abnormal phenomenon that the maximum effective principal stresses decrease with the constant minimum effective pressure, as shown in Figure 13. The essence of this phenomenon is that one effective confining pressure meets the boundless group's pore and confining pressure. The diameter of Mohr's circle decreases with an increase in σ_3 and P_p when the coal samples are at a 3 or 6 MPa effective confining pressure, as shown in Figure 14. Although the maximum and minimum principal stresses of the circles are changing, the tilted tangents of these circles cannot be derived in Figure 14a. The diagram of the failure curves of the circles indicates that the failure curve shifts downward and the slope decreases with increasing confining pressure and pore pressure at a constant effective envelope pressure (Figure 14c). This suggests that both τ and σ_n at the ultimate state are decreased and that the coal is more susceptible to failure.

The new coefficient μ that relates pore pressure and the principal stresses is proposed to characterize the relationship between pore and confining pressure. The coefficient μ reflects the weakening effect of pore pressure on confining pressure at a certain $\sigma^e{}_3$. The coefficient μ is the ratio of pore pressure to confining pressures, as follows.

$$\mu = \frac{\alpha P_p}{\sigma_3} = \frac{\alpha P_p}{\alpha P_p + \sigma_3^e} \tag{13}$$

where $\sigma^e{}_3$ denotes the effective confining pressure, P_p denotes the pore pressure, and α is still 1 in this study. The coefficient μ ranges from 0 to 1, and a higher coefficient μ suggests a lower strength at a certain $\sigma^e{}_3$. Figure 15 shows the theoretical value of coefficient μ when $\sigma^e{}_3$ ranges from 3 to 15 MPa and σ_3 ranges from 0 to 301 MPa. This suggests that the coefficient μ increases sharply when the confining pressure is low at 75 MPa, and the increasing tendency is higher with a decrease in the effective confining pressure. The experimental data (blue stars in Figure 15) indicate the coefficient μ evolution at an effective confining pressure of 6 MPa. The coefficients μ are 0.31, 0.5, and 0.6 when the confining pressures are 9, 12, and 15 MPa, respectively.

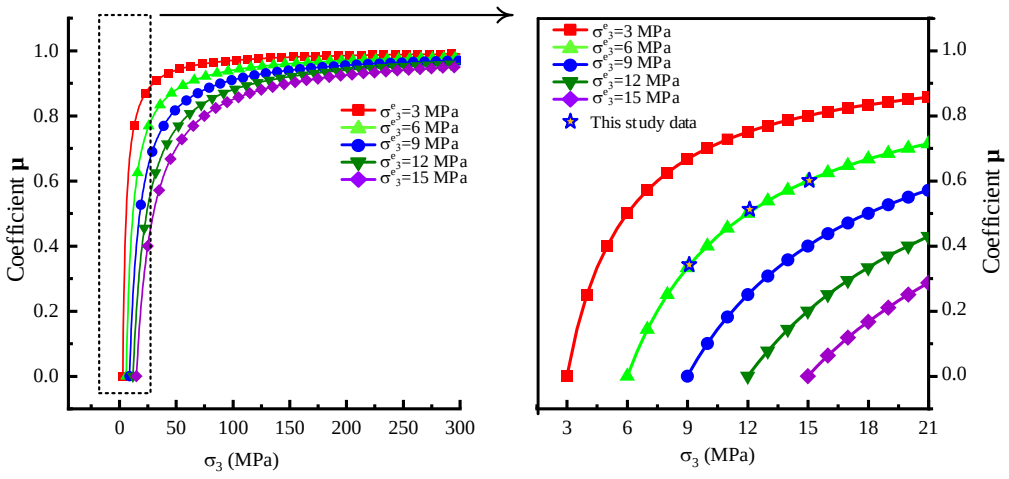

Figure 15. Evolution of coefficient μ at different $\sigma^e{}_3$ values.

Figure 16 illustrates the coefficient μ and the variation in the compressive strength. In this paper, the coefficient μ and the strength of the ZT coal show a nonstandard exponential function relationship at a constant effective confining pressure of 6 MPa. The strength of the coal rock does not change significantly when $\mu < 0.35$, indicating that the strength weakening effect of the pore pressure is small. The compression strength of the coal rock has a significant decreasing trend when $\mu > 0.35$, indicating that the strength weakening effect of the pore water is significant. *A* coefficient μ equal to zero indicates a dry state rather

than a water-saturated but no pore pressure state. In contrast, a coefficient μ equal to 1 indicates that the pore pressure is equal to the minimum principal stress state. We combine the coefficient μ and Mohr–Coulomb criterion to propose Equation (14) to overcome the deficiency in Equation (12).

$$\sigma_1^e = \sigma_3^e(1 - k\mu) + \frac{2[c + \sigma^e{}_3 \tan\phi(1 - k\mu)]}{(1 - \tan\phi\cot\beta)\sin 2\beta} \quad (14)$$

where μ is the coefficient and k is a fitting exponential function in this study. Part of $(1 - k\mu)$ represents a discount in $\sigma^e{}_3$.

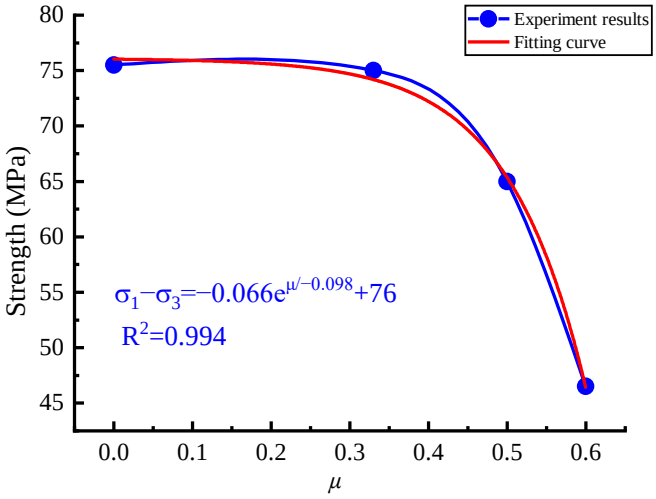

Figure 16. The evolution of strength and the coefficient μ.

3.4. Effect of Pore Pressure on Macrocracks in Coal

3.4.1. Angle Evolution of the Macro Failure Plane

The major failure plane of most coal samples is macro incline shear failure with different dip angles. In addition to incline shear failure, macro vertical tensile cracks and conjugation shear cracks occurred in individual coal samples. To quantitatively describe the effect of pore pressure and confining pressures on the macro failure of coal samples, the angle β of the macro failure plane was measured, which is between the major macro failure plane and the minimum principle stress of the coal samples. Angle β is listed in Table 2.

Table 2. The evolution of the macro failure plane angle β at different confining and pore pressures.

Sample Condition	σ_3 (MPa)	β (°)	Sample Condition	σ_3 (MPa)	β (°)	Sample Condition	σ_3 (MPa)	β (°)
dry	9	64.2	wet	9	68.7	$\sigma^e{}_3$ = 6 MPa	9	67.6
dry	12	63.2	wet	12	64.8	$\sigma^e{}_3$ = 6 MPa	12	69.0
dry	15	56.5	wet	15	64.5	$\sigma^e{}_3$ = 6 MPa	15	70.5
$\sigma^e{}_3$ = 3 MPa	9	64.7	$\sigma^e{}_3$ = 6 MPa	9	53.5			
$\sigma^e{}_3$ = 3 MPa	12	68.4	$\sigma^e{}_3$ = 6 MPa	12	67.6			
$\sigma^e{}_3$ = 3 MPa	15	72.4	$\sigma^e{}_3$ = 6 MPa	15	71.9			

The β of the dry coal sample decreases from 64.2° to 56.5° when the confining pressure increases from 9 to 15 MPa. The evolution of β of the wet coal samples is consistent with that of the dry coal samples, but the β of the wet coal samples is higher than that of dry coal samples at the corresponding confining pressure. This indicates that the confining pressure can facilitate a β decrease, while the pore water can facilitate a β increase. However, the β of the saturated coal sample increases with an increase in confining pressure and pore

pressure when the effective confining pressure remains constant. The reason is that the ratio μ increases with a synchronous increase in pore and confining pressure.

3.4.2. Porous-Rich Layer Effect on Mechanical Behaviors

The porosity distribution of the coal samples in this paper presents two cases: an approximately uniform pore distribution and an obviously horizontal porous-rich layer distribution (Figure 2b). This horizontal porous-rich layer distribution will make coal samples transversely isotropic coal samples and affect the macro crack development.

A single-layer model of the porous-rich layer was developed to further study the effect of the porous-rich layer on macro shear crack development, as shown in Figure 17. The model contains three parts, where Parts 1 and 3 indicate that the coal in this area is predominantly a matrix with few pores. Part 2 indicates that the coal in this area contains many pores. The blue circles denote open pores in the coal, as shown in Figure 17a. For ease of description, stresses are denoted at σ_j^i, where i is the area number and equals 1, 2, 3, and j = 1, 3, j denotes the maximum and minimum principal stresses. The maximum principal stress ${\sigma^1}_1$ of Part 1 is the ratio of the axial force to the cross-area (F/A), while the maximum principal stress ${\sigma^2}_1$ of Part 2 is F/A_1, where A_1 is the effective cross-area of the coal (A subtracts the pore area). It is assumed that A equals $b \times A_0$, and since the maximum porosity of the coal is approximately 10%, b = 0.9.

$$\sigma_1^2 = \frac{F - P_p(1-b)A}{A_1} = \frac{F - P_p(1-b)A}{Ab} \tag{15}$$

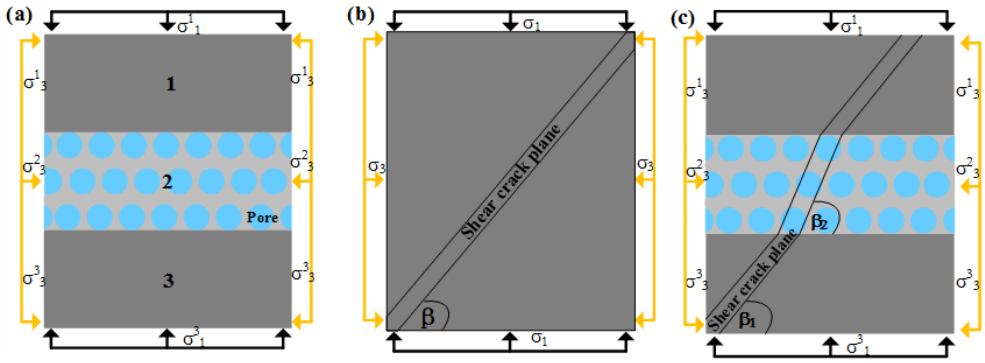

Figure 17. The diagrammatic drawing of the porous-rich layer plane in coal: (**a**) model of coal with a porous-rich layer band; (**b**) macro shear crack in coal without an obvious porous-rich layer band; (**c**) macro shear crack in coal with an obvious porous-rich layer band. σ^i_j denotes the principal stress, where i = 1, 2, 3 denotes Parts 1, 2, and 3, respectively, and j = 1, 3 denotes the maximum and minimum principal stresses, respectively.

After dissolution, the maximum principal stress of Part 2 is as follows:

$$\sigma_1^2 = \frac{F}{Ab} - \frac{P_p}{b} + P_p \tag{16}$$

Substituting ${\sigma^1}_1 = F/A$ and b = 0.9 into Equation (16), ${\sigma^2}_1$ equals $9{\sigma^1}_1 - 8P$p. Furthermore, ${\sigma^2}_1 - {\sigma^1}_1 = 8({\sigma^1}_1 - P$p). Because ${\sigma^1}_1$ is greater than Pp, ${\sigma^2}_1 - {\sigma^1}_1$ is greater than 0. This suggests a disequilibrium on the interface between the adjacent parts, and the axial stress on the porous-rich layer structure surface is greater than that on the nonporous layer surface.

The confining stress ${\sigma^1}_3$ at Part 1 equals ${\sigma^3}_3$ at Part 3. However, the confining pressure ${\sigma^2}_3$ at Part 2 equals ${\sigma^1}_3 - P_P$; i.e., ${\sigma^2}_3$ is lower than ${\sigma^1}_3$. The porous-rich layer leads to different stresses in the parts. This disequilibrium in σ_3 could significantly affect the macrocrack growth such that effective confining facilitates an increase in β. As a result, the

macro failure plane angle β of the crack would increase or decrease through the different parts. Figure 17b shows an ideal model of a macro shear crack developing at a constant angle β. In contrast, Figure 17c shows the model in which the angle β of the macro shear crack increases at the porous-rich layer. This evolution of angle β in the experimental result is shown in Figure 18.

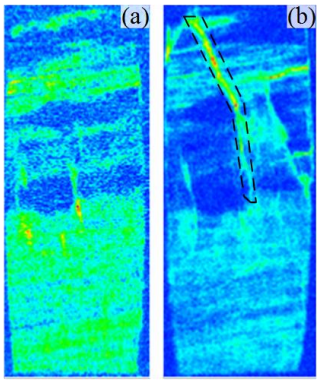

Figure 18. The angle of macrocrack development in the coal sample by NMR scan section: (**a**) original sample; (**b**) failed sample.

3.5. Effect of Pore Pressure on Cracks by AE Analysis

The density kernel of the AE parameters of the coal sample is plotted to quantify the influence of pore pressure on the crack characteristics, as shown in Figure 19. When σ_3 = 9 MPa, at 3 MPa pore pressure, the core of the RA is lower than 3000 ms/v, and the core of AF is lower than 110 kHz. The density kernel of the AE event is under the dividing line. When the pore pressure, P_p, is increased to 6 MPa, the RA in the concentrated region of the parametric density distribution is less than 1700 ms/v, and the RA of the density kernel is reduced by 43% compared with P_p = 3 MPa. The AF is less than 220 kHz, and the AF of the density core increases by 100% compared to P_p = 3 MPa. The AE parameter density kernel (blue–purple part) is up the dividing line.

At a confining pressure of 12 MPa, the AE parameter density kernel also exhibits a similar law. As the pore pressure increases, the AF of the parameter distribution density kernel increases, the RA decreases, and the density kernel moves to the left. It can also be analyzed from the perspective of effective stress. The AE parameter density kernel moves from the bottom right to the upper left when the effective stress is reduced. The movement trend of this density kernel indicates that the proportion of shear cracks in coal rock decreases and the proportion of tensile cracks increases when the pore pressure increases or the confining pressure decreases.

To highlight the tensile and shear characteristics of the cracks, a parameter ratio is proposed. The ratio equals RA/AF. A high ratio represents more significant shear properties of the cracks, while a low ratio represents more significant tensile properties of the cracks. To further analyze the crack evolution of the coal samples under the effect of pore pressure, Figure 20 shows the ratio of RA to AF at each stage of deformation. It is widely known that coal shows five stages of deformation when compressed and deformed: crack closure (I), elastic region (II), stable crack growth (III), unstable crack growth (IV), and postpeak stages (V) under compression.

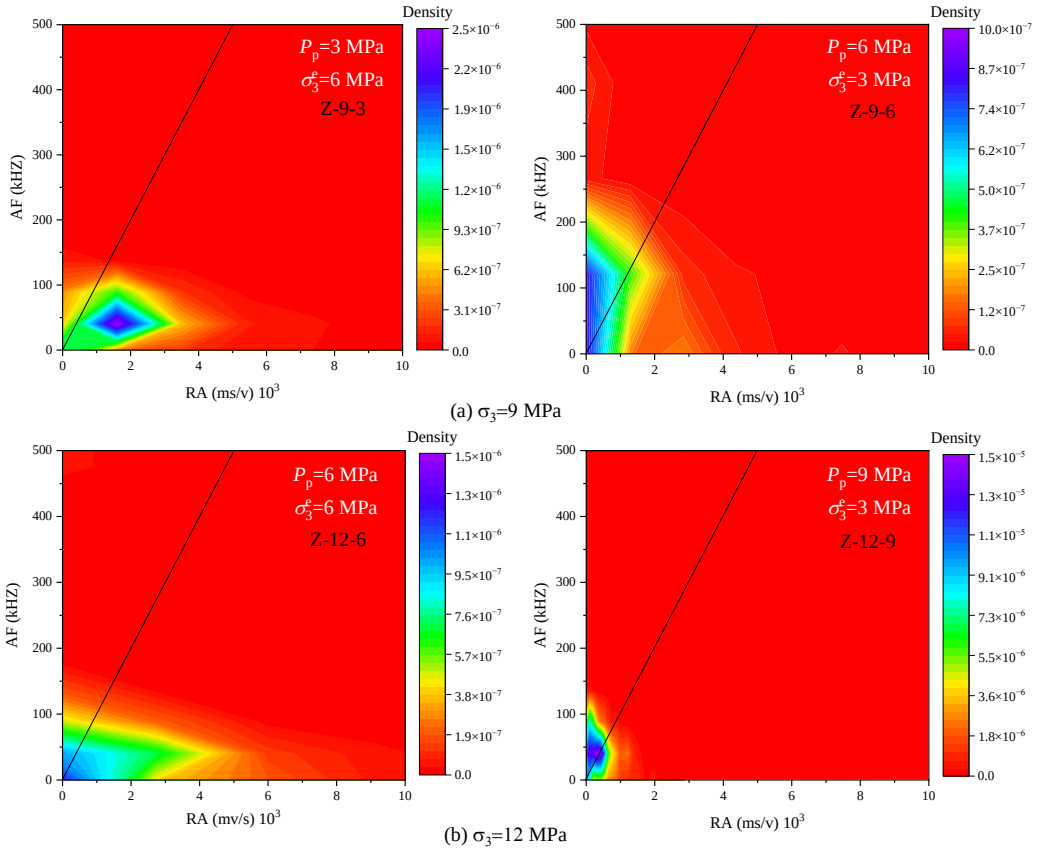

Figure 19. AE parameter density kernel evolution at confining pressures of 9 and 12 MPa.

Figure 20 shows the evolution of the ratio of the dry and saturated coal samples in different deformation stages. In the absence of pore pressure, the AE signal of the coal samples in the first three stages is very few. At a confining pressure of 9 MPa, no signal was collected in the first three stages (Figure 20b). When subjected to pore pressure, the AE activity increased significantly. This increase was very significant in the first three stages. This is due to the action of the pore water, making it easy for microcracks to conceive and expand. Throughout the compression process, the ratio of the first three stages is small, which indicates that the cracking in the I, II, and II stages is dominated by tensile micro cracking. There is a large increase in the ratio during the IV stage, indicating a significant increase in shear cracking. The ratio increases significantly in the V stage, indicating a significant increase in shear cracking.

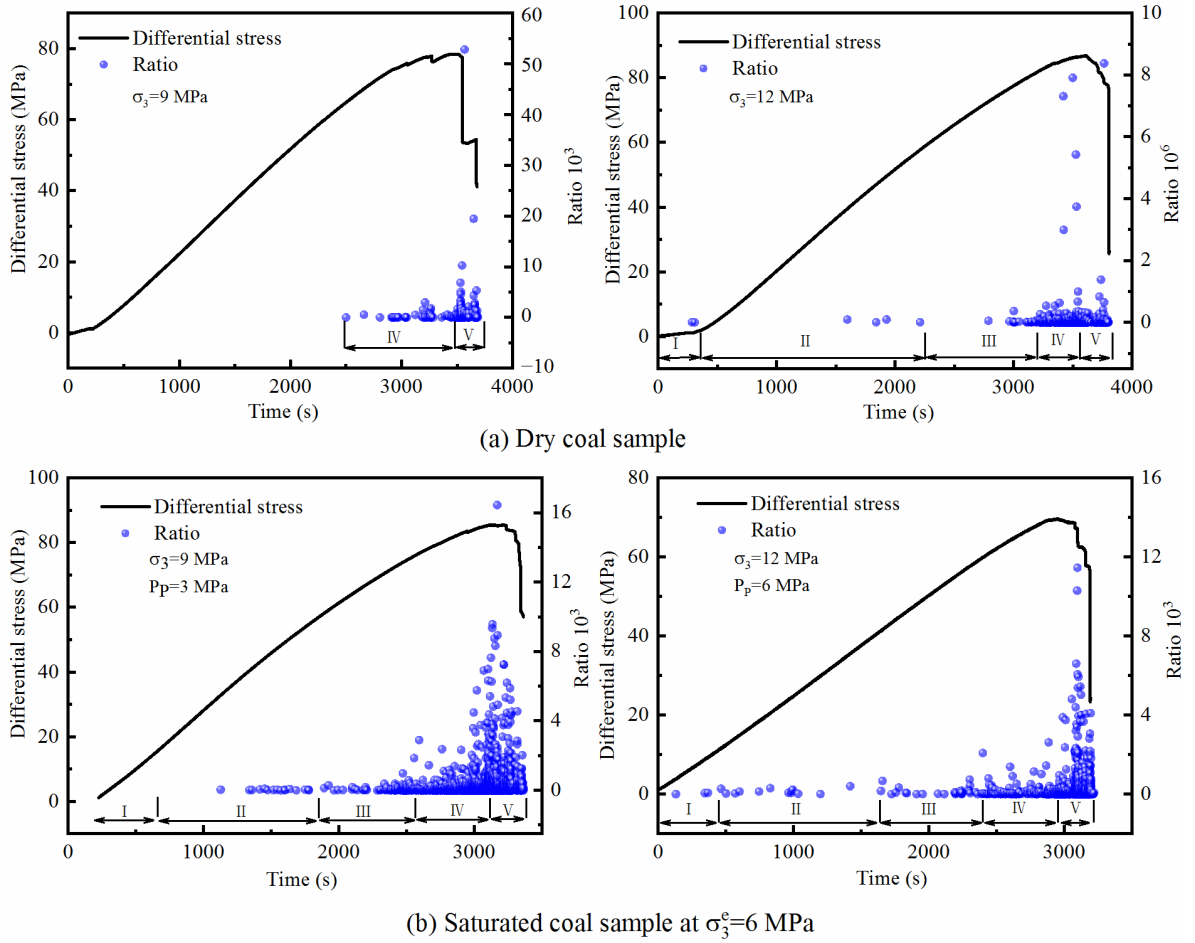

Figure 20. Evolution of the ratio of dry and saturated coal samples in different deformation stages.

4. Discussion

With increasing depth, both the ground stress and pore pressure increase significantly. The effect of pore pressure on the strength and elastic modulus is inversely related to that of the confining stress. We therefore investigated the evolution of the mechanical parameters when the pore pressure and the confining pressure increased simultaneously. The pore pressure setting in this paper is relatively high compared to other studies [26,40–42], and this is one of the features of this paper. In fact, phenomena of abnormal pore pressures are found in many regions of the world, e.g., the US, France, and Iran [43]. Figure 21 shows a schematic diagram of stress and abnormal pore pressure. The dashed box in Figure 21 is the stress condition studied in this paper. There is a simultaneous increase in pore pressure and confining pressure in these cases. Furthermore, this paper investigates the evolution of the mechanical parameters at constant effective stress and improves the perception in these cases. Considering the ground stresses in coal seam mining, the confining pressure in this paper is not very high; therefore, the mechanical parameters at ultrahigh confining stresses require further experimental investigation.

The effect of pore pressure on coal burst is not considered in conventional bursts in shallow coal seams. However, when the coal seam is mined at deeper depths, the permeability of the seam is lower, adsorption is high, and the pore pressure within the seam is higher than those of shallow coal seams [2,17,19]. Therefore, the effect of pore pressure on the dynamic destabilization of coal must be considered. According to the results of our study, the elastic modulus and strength of a coal seam increase when the pore pressure is decreased. This will result in an increased risk of burst in the coal seam [44,45]. When combating gas outbursts or compound dynamic disasters, the extraction of geological fluids

must be maintained at an appropriate volume. A significant decrease in pore pressure is not the best approach and should result in the pore pressure being maintained at a suitable value [46].

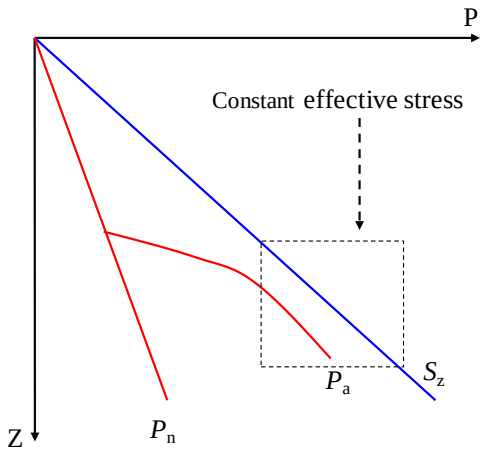

Figure 21. Schematic diagram of stress and abnormal pore pressure [47]. Z is the depth, P is the pressure, S_z denotes the overlay stress, P_n denotes the normal pore pressure, and P_a denotes the abnormal pore pressure.

According to the law of evolution of β in Section 3.4, the angle of β increases with increasing pore pressure at a confining pressure. This indicates that as the pore pressure increases, the macroscopic failure cracks in the coal shift from shear cracks to tension cracks. At constant effective stress, the angle of β increases with simultaneous increases in the pore and confining pressures. This result is also demonstrated by the AE monitoring results, as shown in Figure 19. As the pore pressure increases, the AE density kernel moves from the bottom right to the upper left. This indicates a gradual increase in tensile cracking and a gradual decrease in shear cracking in coal. Both the AE analysis and the macroscopic failure angle analysis consistently show the effect of pore pressure on crack extension in coal.

5. Conclusions

The volume strain curve exhibits a semilunar shape when there is no influence of pore pressure, while most of the volume strain curve is linear and the yield stage of burst tendency coal is short or nonexistent under the pore pressure effect.

The elastic modulus and strength of a coal seam increase when the pore pressure is decreased. This results in an increased risk of burst in the coal seam. However, the elastic modulus and compressive strength decrease with an increase in confining pressure and pore pressure simultaneously. This is mainly due to the coefficient μ (the ratio of pore pressure to confining pressures) increasing. The Mohr–Coulomb criterion is modified to propose the Mohr–Coulomb criterion containing coefficient μ, which improves the expression of effective stress in the Mohr–Coulomb criterion. When combating gas outbursts or compound dynamic disasters, the extraction of geological fluids must be maintained at an appropriate volume. A significant decrease in pore pressure is not the best approach and should result in the pore pressure being maintained at a suitable value.

The macro shear failure angle of dry and wet coal samples decreases with an increase in confining pressure. In contrast, the angle increases with both confining pressure and pore pressure. The porous-rich layer affects the macroscopic shear crack propagation angle. A model was developed to illustrate the imbalance in the effective stresses due to the presence of porous-rich layers. This single pore-rich layer model is based on a small-scale laboratory model. Further research is needed on multilayer porous and large-scale models for application in real coal seams.

Author Contributions: Conceptualization, methodology, review and editing, K.X.; writing—review and editing, X.L.; formal analysis, data curation, Y.L. (Yanan Liu); data curation, review and editing, Y.L. (Yong Luo) and Z.L.; writing—original draft preparation, K.L. All authors have read and agreed to the published version of the manuscript.

Funding: This research was funded by the National Natural Science Foundation of China, grant numbers 51674047 and 51911530152.

Institutional Review Board Statement: Not applicable.

Informed Consent Statement: Not applicable.

Data Availability Statement: Not applicable.

Conflicts of Interest: The authors declare no conflict of interest.

Appendix A

The derivation of the Mohr–Coulomb criterion in the form of principal stress.

$$\begin{cases} \tau = \frac{(\sigma_1-\sigma_3)}{2}\sin 2\beta \\ \sigma_n = \frac{\sigma_1+\sigma_3}{2} + \frac{(\sigma_1-\sigma_3)}{2}\cos(2\beta) \end{cases} \tag{A1}$$

$$\tau = c + \sigma_n \tan(\phi) \tag{A2}$$

Substituting Equation (A1) into Equation (A2):

$$\begin{gathered} \tfrac{(\sigma_1-\sigma_3)}{2}\sin 2\beta = c + \tfrac{(\sigma_1+\sigma_3)}{2}\tan\phi + \tfrac{(\sigma_1-\sigma_3)}{2}\cos 2\beta\tan\phi \\ \sigma_1\sin 2\beta - \sigma_3\sin 2\beta = 2c + \sigma_1\tan\phi + \sigma_3\tan\phi + \sigma_1\cos 2\beta\tan\phi - \sigma_3\cos 2\beta\tan\phi \\ \sigma_1\sin 2\beta - \sigma_1\tan\phi - \sigma_1\cos 2\beta\tan\phi = 2c + \sigma_3\sin 2\beta + \sigma_3\tan\phi - \sigma_3\cos 2\beta\tan\phi \\ \sigma_1(\sin 2\beta - \tan\phi - \cos 2\beta\tan\phi) = 2c + \sigma_3(\sin 2\beta + \tan\phi - \cos 2\beta\tan\phi) \\ \sigma_1[\sin 2\beta - \tan\phi(1+\cos 2\beta)] = 2c + \sigma_3[\sin 2\beta + \tan\phi(1-\cos 2\beta)] \\ \sigma_1(\sin 2\beta - 2\tan\phi\cos^2\beta) = 2c + \sigma_3(\sin 2\beta + 2\tan\phi\sin^2\beta) \\ \sigma_1(\sin 2\beta - 2\tan\phi\cos^2\beta) = 2c + \sigma_3(\sin 2\beta - 2\tan\phi\cos^2\beta + 2\tan\phi\cos^2\beta + 2\tan\phi\sin^2\beta) \\ \sigma_1(\sin 2\beta - 2\tan\phi\cos^2\beta) = 2c + \sigma_3(\sin 2\beta - 2\tan\phi\cos^2\beta + 2\tan\phi) \\ \sigma_1 = \frac{2c}{\sin 2\beta - 2\tan\phi\cos^2\beta} + \frac{\sigma_3(\sin 2\beta - 2\tan\phi\cos^2\beta + 2\tan\phi)}{\sin 2\beta - 2\tan\phi\cos^2\beta} \\ \sigma_1 = \frac{2c}{\sin 2\beta - 2\tan\phi\cos^2\beta} + \frac{2\sigma_3\tan\phi}{\sin 2\beta - 2\tan\phi\cos^2\beta} + \sigma_3 \\ \sigma_1 = \sigma_3 + \frac{2(c+\sigma_3\tan\phi)}{\sin 2\beta(1-\tan\phi\cot\beta)} \end{gathered}$$

References

1. Wang, K.; Du, F. Coal-gas compound dynamic disasters in China: A review. *Process Saf. Environ. Prot.* **2020**, *133*, 1–17. [CrossRef]
2. Pan, Y.S. Integrated study on compound dynamic disaster of coal-gas outburst and rockburst. *J. China Coal Soc.* **2016**, *41*, 105–112.
3. Qing, Q.X.; Pan, Y.S.; Li, H.T.; Jiang, D.Y.; Shu, L.Y.; Zhao, S.K.; Zhang, Y.J.; Pan, J.F.; Hongyan, L.; Pan, P.Z. Theoretical basis and key technology of prevention and control of coal-rock dynamic disasters in deep coal mining. *J. China Coal Soc.* **2020**, *45*, 1567–1584.
4. Wang, K.; Du, F.; Zhang, X.; Wang, L.; Xin, C. Mechanical properties and permeability evolution in gas-bearing coal–rock combination body under triaxial conditions. *Environ. Earth Sci.* **2017**, *76*, 815. [CrossRef]
5. Li, T.; Cai, M.F.; Cai, M. A review of mining-induced seismicity in China. *Int. J. Rock Mech. Min. Sci.* **2007**, *44*, 1149–1171. [CrossRef]
6. Yin, G.; Qin, H.; Huang, G.; Lv, Y.; Dai, Z. Acoustic emission from gas-filled coal under triaxial compression. *Int. J. Min. Sci. Technol.* **2012**, *22*, 775–778. [CrossRef]
7. Xue, S.; Zheng, C.; Zheng, X.; Jiang, B.; Li, Y.; Wang, Z. Experimental determination of the outburst threshold value of energy strength in coal mines for mining safety. *Process Saf. Environ. Prot.* **2020**, *138*, 263–268. [CrossRef]
8. Du, F.; Wang, K.; Wang, G.; Jiang, Y.; Xin, C.; Zhang, X. Investigation of the acoustic emission characteristics during deformation and failure of gas-bearing coal-rock combined bodies. *J. Loss Prev. Process Ind.* **2018**, *55*, 253–266. [CrossRef]
9. Masoudian, M.S.; Airey, D.W.; El-Zein, A. Experimental investigations on the effect of CO_2 on mechanics of coal. *Int. J. Coal Geol.* **2014**, *2014. 128*, 12–23. [CrossRef]

10. Niu, Y.; Li, Z.; Wang, E.; Gao, F.; Wang, F.; Zhang, Z.; Deng, Q.; Long, Z.; Zhang, X.; Tian, H. An experimental study on precursor identification for gas-bearing coal failure from electric potential responses in the loading process. *Meas. J. Int. Meas. Confed.* **2022**, *196*, 111229. [CrossRef]
11. Wang, C.; Xu, X.; Zhang, Y.; Arif, M.; Wang, Q.; Iglauer, S. Experimental and numerical investigation on the dynamic damage behavior of gas-bearing coal. *Geomech. Geophys. Geo-Energy Geo-Resour.* **2022**, *8*, 49. [CrossRef]
12. Liu, S.; Li, X.; Wang, D.; Zhang, D. Investigations on the mechanism of the microstructural evolution of different coal ranks under liquid nitrogen cold soaking. *Energy Sources Part A Recovery Util. Environ. Eff.* **2020**, 1–17. [CrossRef]
13. Zhang, C.; Wang, E.; Li, B.; Kong, X.; Xu, J.; Peng, S.; Chen, Y. Laboratory experiments of CO_2-enhanced coalbed methane recovery considering CO2 sequestration in a coal seam. *Energy* **2022**, *262*, 125473. [CrossRef]
14. Luo, P.; Zhang, Z.; Geng, X.; Xue, K.; Guang, W. Evaluation of $ScCO_2$-water performance on bituminous coal: Insights from experiments and 3D CT image reconstruction. *Geomech. Geophys. Geo-Energy Geo-Resour.* **2022**, *8*, 118. [CrossRef]
15. Kang, H.; Yi, B.; Gao, F.; Lü, H. Database and characteristics of underground in situ stress distribution in chinese coal mines. *J. China Coal Soc.* **2019**, *44*, 23–33.
16. Guang, W.; Liu, X.; Zhang, Z.; Luo, P. Effects of sub-and supercritical CO_2 on coal diffusivity and surface Thermodynamics. *Energy Fuels* **2022**, *36*, 3737–3748. [CrossRef]
17. Xue, K.; Zhang, Z.; Zhong, C.; Jiang, Y.; Geng, X. A fast numerical method and optimization of 3D discrete fracture network considering fracture aperture heterogeneity. *Adv. Water Resour.* **2022**, *162*, 104164. [CrossRef]
18. Wang, Y.; Zhang, Z.; Ranjith, P.G.; Luo, Y. Water-gas flow in rough rock fractures: Insights from coupled triaxial compression experiments. *Hydrogeol. J.* **2022**, *30*, 1569–1581. [CrossRef]
19. Zhang, C.; Wang, E.; Xu, J.; Peng, S. A new method for coal and gas outburst prediction and prevention based on the fragmentation of ejected coal. *Fuel* **2021**, *287*, 119493. [CrossRef]
20. Ning, J.; Wang, J.; Jiang, J.; Hu, S.; Jiang, L.; Liu, X. Estimation of crack initiation and propagation thresholds of confined brittle coal specimens based on energy dissipation theory. *Rock Mech. Rock Eng.* **2017**, *51*, 119–134. [CrossRef]
21. Long, K.; Zhang, Z.; Li, S.; Li, K.; Luo, Y. The roles of crack development and water in stress rotation and fault weakening. *Tectonophysics* **2022**, *823*, 229190. [CrossRef]
22. Ranathunga, A.S.; Perera, M.S.A.; Ranjith, P.G. Influence of CO_2 adsorption on the strength and elastic modulus of low rank Australian coal under confining pressure. *Int. J. Coal Geol.* **2016**, *167*, 148–156. [CrossRef]
23. Li, X.; Chen, S.; Wang, S.; Zhao, M.; Liu, H. Study on in Situ Stress Distribution Law of the Deep Mine: Taking Linyi Mining Area as an Example. *Adv. Mater. Sci. Eng.* **2021**, *2021*, 5594181. [CrossRef]
24. Zhang, Z.; Xie, H.; Zhang, R.; Zhang, Z.; Gao, M.; Jia, Z.; Xie, J. Deformation damage and energy evolution characteristics of coal at different depths. *Rock Mech. Rock Eng.* **2019**, *52*, 1491–1503. [CrossRef]
25. Yang, S.Q.; Jing, H.W.; Cheng, L. Influences of pore pressure on short-term and creep mechanical behavior of red sandstone. *Eng. Geol.* **2014**, *179*, 10–23. [CrossRef]
26. Han, B.; Shen, W.Q.; Xie, S.Y.; Shao, J.F. Influence of pore pressure on plastic deformation and strength of limestone under compressive stress. *Acta Geotech.* **2019**, *14*, 535–545. [CrossRef]
27. Terzaghi, K.T. *Theoretical Soil Mechanics*; John Wiley and Sons Inc.: New York, NY, USA, 1943; p. 314.
28. Biot; Maurice, A. General theory of three-dimensional consolidation. *J. Appl. Phys.* **1941**, *12*, 155–164. [CrossRef]
29. Saurabh, S.; Harpalani, S. The effective stress law for stress-sensitive transversely isotropic rocks. *Int. J. Rock Mech. Min. Sci.* **2018**, *101*, 69–77. [CrossRef]
30. Wang, Y.; Meng, F.; Wang, X.; Baud, P.; Wong, T.F. Effective stress law for the permeability and deformation of four porous limestones. *J. Geophys. Res. Solid Earth* **2018**, *123*, 4707–4729. [CrossRef]
31. Zhang, L.; Kan, Z.; Zhang, C.; Tang, J. Experimental study of coal flow characteristics under mining disturbance in China. *Int. J. Coal Sci. Technol.* **2022**, *9*, 66. [CrossRef]
32. Sing, K.S.W. Reporting physisorption data for gas/solid systems with special reference to the determination of surface area and porosity (Recommendations 1984). *Pure Appl. Chem.* **1985**, *57*, 603–619. [CrossRef]
33. Culshaw, M.G.; Ulusay, R. The ISRM suggested methods for rock characterization, testing and monitoring: 2007–2014: Cham, Switzerland: Springer. *Bull. Eng. Geol. Environ.* **2015**, *74*, 1499–1500. [CrossRef]
34. Liu, Y.; Wang, J.H.; Lu, C.P.; Wang, C.; Xie, H.D.; Yan, X.Y. Research on instability characteristics and precursory effect of coal-rock parting-coal structures. *Sci. Rep.* **2022**, *12*, 12091. [CrossRef] [PubMed]
35. Noorsuhada, M.N. An overview on fatigue damage assessment of reinforced concrete structures with the aid of acoustic emission technique. *Constr. Build. Mater.* **2016**, *112*, 424–439. [CrossRef]
36. Ohno, K.; Ohtsu, M. Crack classification in concrete based on acoustic emission. *Constr. Build. Mater.* **2010**, *24*, 2339–2346. [CrossRef]
37. Yao, Q.; Chen, T.; Tang, C.; Sedighi, M.; Wang, S.; Huang, Q. Influence of moisture on crack propagation in coal and its failure modes. *Eng. Geol.* **2019**, *258*, 105156. [CrossRef]
38. Martin, C.D.; Chandler, N.A. The Progressive fracture of Lac du Bonnet granite. *Int. J. Rock Mech. Min. Sci. Geomech. Abstr.* **1994**, *31*, 643–659. [CrossRef]
39. Nicksiar, M.; Martin, C.D. Evaluation of methods for determining crack initiation in compression tests on low-porosity rocks. *Rock Mech. Rock Eng.* **2012**, *45*, 607–617. [CrossRef]

40. Han, B.; Xie, S.Y.; Shao, J.F. Experimental investigation on mechanical behavior and permeability evolution of a porous limestone under compression. *Rock Mech. Rock Eng.* **2016**, *49*, 3425–3435. [CrossRef]
41. Zhang, B.; Wu, H.; Liu, C.; Han, F.; Ma, Y. The effect of stress on pore pressure in rocks and the mechanism of water table anomaly before earthquakes. *Acta Seismol. Sin.* **1992**, *5*, 153–159. [CrossRef]
42. Wong, T.F.; David, C.; Zhu, W. The transition from brittle faulting to cataclastic flow in porous sandstones; mechanical deformation. *J. Geophys. Res. Solid Earth* **1997**, *102*, 3009–3025. [CrossRef]
43. Rubey, W.W.; King, H.M. Role of fluid pressure in mechanics of overthrust faulting: II overthrust belt in geosybclinal area of western Wyoming in light of fluid-pressure hypothesis. *GSA Bull.* **1959**, *70*, 167–206. [CrossRef]
44. Luo, H.; Yu, J.K.; Pan, Y.S.; Wang, J.L.; Zhang, Y. Electric charge induction law of coal rock containing gas with bursting tendency during loading failure process. *J. China Coal Soc.* **2020**, *45*, 684–694.
45. Song, Z.L.; Han, P.B.; Li, W.P.; Yin, G.Z.; Li, M.H.; Kang, X.T. Impact of energy dissipation of coal samples with rockburst tendency from gas in its failure process. *J. China Coal Soc.* **2015**, *40*, 843–849.
46. Qing, Q.X.; Pan, Y.S.; Shu, L.Y.; Li, H.Y.; Jiang, D.Y.; Zhao, S.K.; Zou, Y.H.; Pan, J.F.; Wang, K.J.; Li, H.T. Theory and technical framework of prevention and control with different sources in multi-scales for coal and rock dynamic disasters in deep mining of coal mines. *J. China Coal Soc.* **2018**, *43*, 1801–1810.
47. Gretener, P.E. *Pore Pressure: Fundamentals, General Ramifications and Implications for Structural Geology (Revised Edition)*; American Association of Petroleum Geologists United States: Tulsa, OK, USA, 1979.